RSC Advances

PAPER

View Article Online
View Journal | View Issue

Cite this: *RSC Adv.*, 2026, **16**, 26546

Genipin-crosslinked CeO_2-incorporating Janus patch for oral ulcer treatment

Han Sol Kim,†[a] Sujin Park,†[b] Shazid Md. Sharker,[c] Sang-woo Lee *[bd] and Ji Hyun Ryu *[aefg]

Oral ulcers and mucositis are difficult to manage clinically due to the persistently wet oral environment, continuous mechanical stress, and the complex inflammatory and oxidative microenvironment at lesion sites. Conventional topical therapies, including corticosteroid gels, often suffer from poor mucosal retention and limited therapeutic durability. Here, we report a dual-layered Janus oral patch that integrates wet-tissue adhesion, localized corticosteroid delivery, and genipin-crosslinked CeO_2 nanozyme-mediated redox regulation for effective oral ulcer treatment. The patch comprises a tissue-facing adhesive layer of gallic acid-conjugated chitosan (CHI-G) loaded with triamcinolone acetonide, and an opposing, non-adhesive outer layer in which CeO_2 nanozymes are immobilized within a genipin-crosslinked CHI-G network. This spatially organized architecture enables stable mucosal fixation while minimizing nonspecific adhesion and nanoparticle leaching. The Janus patch exhibited strong adhesion to wet oral mucosa, resistance to salivary shear flow, and effective barrier function against bacterial penetration. *In vitro* and *in vivo* biosafety assessments confirmed excellent biocompatibility and the absence of systemic cerium accumulation. In a mouse oral ulcer model, the dual-layered Janus patch significantly accelerated wound closure compared to untreated and conventional corticosteroid gel-treated controls. Histological and immunohistochemical analyses revealed enhanced re-epithelialization, reduced inflammatory cell infiltration, and significant reduction of oxidative stress at the ulcer site. Collectively, genipin-stabilized CeO_2 nanozyme-integrated Janus patch design provides a robust and localized therapeutic strategy for oral ulcers, offering a clinically relevant platform that overcomes key limitations of conventional treatments.

Received 11th January 2026
Accepted 23rd April 2026

DOI: 10.1039/d6ra00275g

rsc.li/rsc-advances

Introduction

Oral ulcers, including recurrent aphthous stomatitis, chemotherapy- or radiotherapy-induced oral mucositis, and trauma-associated mucosal lesions, constitute a prevalent and clinically challenging group of disorders that substantially impair patients' quality of life through pain, dysphagia, and increased susceptibility to secondary infection.[1–3] At the lesion site, compromised epithelial barrier function together with dysregulated host immune responses creates a pro-inflammatory and oxidative microenvironment that leads to delayed wound healing and secondary infection.[4,5] Within this pathological context, current clinical management strategies for oral ulcers and mucositis remain largely palliative. Topical corticosteroids such as triamcinolone acetonide (TA) are widely prescribed to suppress inflammatory signaling and alleviate pain.[3,6] However, conventional dosage forms (*e.g.*, gels, ointments, mouth rinses) often exhibit limited efficacy because drug residence time on the mucosa is short in the persistently moist oral cavity and mechanical forces from tongue motion, mastication, and swallowing.[7,8] As a result, repeated administration is frequently required, raising concerns about prolonged glucocorticoid exposure, which is known to disrupt multiple phases of wound healing, including angiogenesis and extracellular matrix remodeling.[9,10] Moreover, oxidative stress has been implicated in the pathogenesis of both recurrent aphthous stomatitis and mucositis, suggesting that redox modulation is required in addition to anti-inflammatory therapy to promote durable healing.[1,11,12]

[a]*Department of Biomedical Materials Science, Graduate School of JABA, Wonkwang University, Iksan, Jeonbuk 54538, Republic of Korea. E-mail: jhryu4816@wku.ac.kr*
[b]*Department of Physiology, School of Dentistry and Dental Research Institute, Seoul National University, Seoul 03080, Republic of Korea. E-mail: goodman23@snu.ac.kr*
[c]*Department of Pharmaceutical Sciences, North South University, Dhaka 1229, Bangladesh*
[d]*Center for Nanoparticle Research, Institute for Basic Science (IBS), Seoul 08826, Republic of Korea*
[e]*Department of Chemical Engineering, Wonkwang University, Iksan, Jeonbuk 54538, Republic of Korea*
[f]*Department of Carbon Convergence Engineering, Wonkwang University, Iksan, Jeonbuk 54538, Republic of Korea*
[g]*Smart Convergence Materials Analysis Center, Wonkwang University, Iksan, Jeonbuk 54538, Republic of Korea*
† These authors contributed equally.

Accordingly, there is increasing interest in localized delivery platforms that can (i) adhere robustly to wet mucosa, (ii) conform to irregular ulcer topography, and (iii) provide a protective barrier against saliva and microbial challenge while enabling sustained local pharmacotherapy.[5,7,8,13] Among these, bioadhesive hydrogels inspired by mussel adhesion or plant polyphenol chemistry have emerged as particularly attractive candidates, as they can achieve robust adhesion under wet conditions through catechol- or gallol-mediated interactions, hydrogen bonding, and metal coordination.[14] Chitosan, a naturally derived polysaccharide with favorable biocompatibility and wound-healing properties, has been extensively explored for oral applications; however, its intrinsic adhesive strength remains insufficient for stable fixation on moist and irregular mucosal surfaces.[14,15] Chemical conjugation of phenolic moieties such as gallic acid to chitosan backbones has been shown to markedly enhance wet-tissue adhesion, enabling intimate contact with ulcer beds and improving local drug delivery efficiency.[16] While improved adhesion addresses one critical limitation of topical therapies, effective management of oral ulcers also requires direct modulation of oxidative stress, which plays a central role in sustaining inflammation and delaying tissue regeneration.[12,17] In this regard, antioxidant nanozymes – nanomaterials that mimic endogenous antioxidant enzymes – offer distinct advantages over conventional small-molecule antioxidants due to their catalytic efficiency and sustained activity.[18,19] Among them, cerium oxide (CeO_2) nanozymes are particularly notable for their reversible redox cycling between Ce^{3+} and Ce^{4+} states, enabling continuous scavenging of superoxide radicals and hydrogen peroxide.[20] Recent studies have demonstrated that locally delivered ceria nanozymes can attenuate oxidative stress, suppress inflammatory cascades, and promote angiogenesis and tissue repair in oral ulcer models.[5,21] Nevertheless, the direct application of nanozymes to oral mucosa raises important concerns regarding uncontrolled particle release, nonspecific tissue adhesion, and potential systemic absorption *via* compromised oral mucosa.[20,22]

To achieve highly localized therapeutic activity with controlled exposure, layered and compartmentalized biomaterial architectures have emerged as a promising design strategy.[23] By spatially separating functional components, such systems allow distinct therapeutic roles to be integrated while minimizing adverse interactions. In oral applications, a dual-layer design can enable intimate contact and drug delivery at the ulcer bed while simultaneously providing a protective or regulatory outer layer that controls exposure of embedded materials and mechanical interaction with non-specific oral mucosa.[5,24,25] Herein, we developed a Janus-surface, dual-layered oral patch designed to address both the delivery challenges and the ROS-rich microenvironment of oral ulcers (Scheme 1). The patch features functionally asymmetric interfaces, comprising a tissue-adaptive adhesive surface that enables stable fixation and localized release of TA, and an opposing, non-adhesive surface capturing CeO_2 nanozymes that provides controlled ROS scavenging while limiting nonspecific mucosal interaction. This spatially organized Janus architecture integrates adhesion, microenvironmental regulation, and barrier protection within a single platform, offering a clinically relevant strategy for oral ulcer treatment.

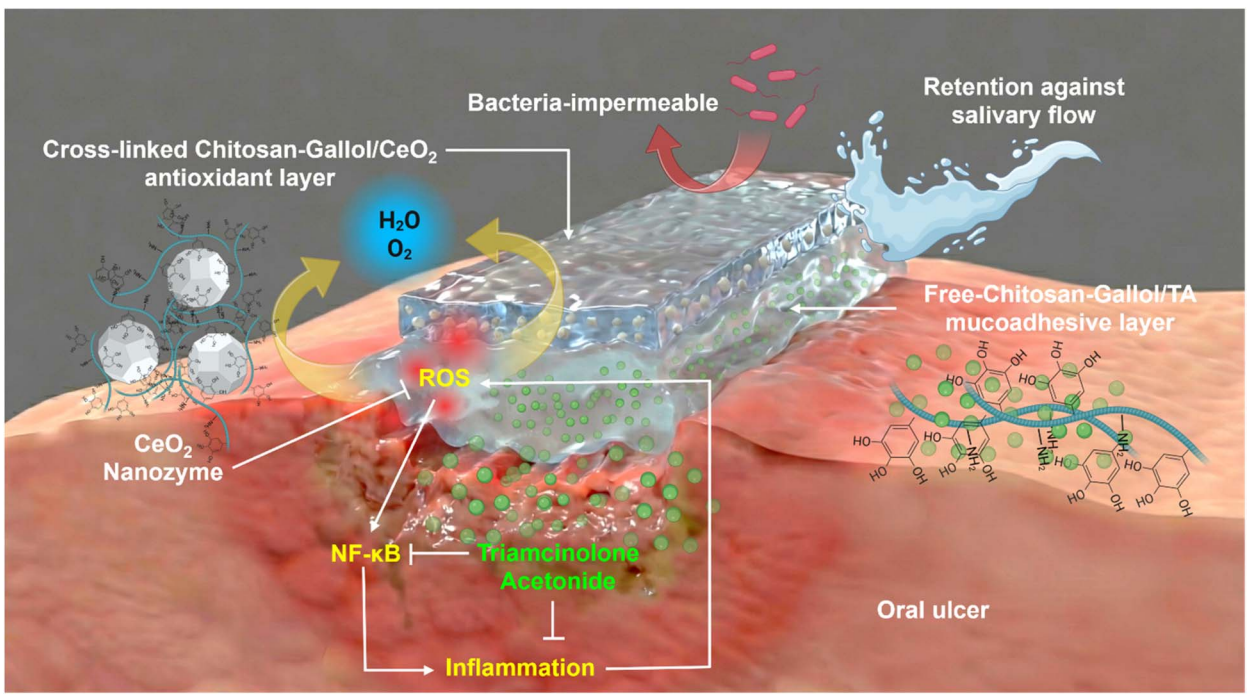

Scheme 1 Schematic illustrations of Janus-surface, dual-layered oral patch.

Experimental sections

Materials

Chitosan (medium molecular weight, 200–800 cP), gallic acid, and cerium(IV) oxide nanoparticles (CeO_2 NPs, particle size <25 nm), acetic acid (≥99.9%), Calcein AM solution (≥90%), propidium iodide (≥94%) and triamcinolone acetonide (TA) were purchased from Sigma-Aldrich (USA). Genipin, 1-ethyl-3-(3-dimethylaminopropyl)carbodiimide hydrochloride (EDC), *N*-hydroxysuccinimide (NHS), and dimethyl sulfoxide (DMSO) were purchased from Tokyo Chemical Industry (TCI, Japan). Hydrochloric acid (HCl), sodium hydroxide (NaOH), and ethanol (Daejung Chemical, Siheung, Republic of Korea) were used as received. For antioxidant evaluation, a commercial DPPH antioxidant assay kit (OxiTec™ DPPH Antioxidant Assay Kit, BIOMAX) was used according to the manufacturer's instructions. Dulbecco's Modified Eagle Medium (DMEM), antibiotic-antimycotic (100×), fetal bovine serum (FBS) and pH 7.4 PBS were purchased from Thermo Fisher Scientific. All other chemicals were of analytical grade and used without further purification.

Synthesis of gallic acid-conjugated chitosan (CHI-G)

CHI-G was synthesized *via* carbodiimide chemistry. Briefly, chitosan (1 g) was hydrated in 1 N HCl (5 mL) for 30 min, followed by the addition of distilled and deionized water (DDW, 75 mL). The pH of the solution was adjusted to 5.0 using 5 N NaOH, yielding a homogeneous chitosan solution. Gallic acid (1 g), EDC (1.2 g), and NHS (0.7 g) were dissolved in a mixed solvent of ethanol and DDW (1 : 3, v/v, 20 mL) and slowly added to the chitosan solution under continuous stirring. The solutions were reacted for 12 h at room temperature, while maintaining the pH at 5.0. The product was purified by dialysis using a membrane (MWCO 12–14 kDa, SpectraPor, USA) against an acidic NaCl solution (pH 2.0) for 2 days, followed by dialysis against DDW for an additional 4 h. The CHI-G was obtained by lyophilization and stored in a desiccator until use. The conjugation of gallic acid to chitosan was confirmed by both ^{1}H NMR (Bruker Avance III, 500 MHz, Billerica, MA, USA) and UV-Vis spectroscopy (UV-2450, Z-202201147260; Shimadzu, Japan) at the Core Facility for Supporting Analysis & Imaging of Biomedical Materials, Wonkwang University, supported by the National Research Facilities and Equipment Center (NFEC). The degree of gallic acid substitution was determined by comparing the absorbance of CHI-G (0.5 mg mL^{-1}) at 265 nm with standard curves of gallic acid concentrations generated from standard solutions (0.001–0.1 mg mL^{-1}) of gallic acid. The degree of gallic acid substitution (DS) of CHI-G was estimated to be 7.5%. In addition, CHI-G with a DS value of 3.7% was synthesized to optimize the formation of the hydrogels.

Preparation of CeO_2 NPs-embedded CHI-G (CHI-G/CeO_2/Gp) hydrogels crosslinked by genipin

CHI-G/CeO_2/Gp hydrogels were prepared by dissolving CHI-G in a pH 7.4 PBS solution, followed by the sequential addition of CeO_2 and genipin. Briefly, CHI-G (2.5 wt%) was dissolved in pH 7.4 PBS solution, genipin was dissolved in DMSO, and CeO_2 (0.5 wt%) NPs were dispersed in pH 7.4 PBS solution, respectively. The CeO_2 (0.5 wt%) NPs were added to the CHI-G solution with vigorous mixing, and the genipin solution was added to the CHI-G/CeO_2 mixture solutions. The volume ratio of CHI-G : CeO_2 : genipin was fixed at 8 : 1 : 1, and the solutions were thoroughly mixed to obtain the final hydrogel formulation. The resulting mixture was poured into a mold, frozen at −80 °C, and subsequently lyophilized. The final concentrations of CHI-G, genipin, and CeO_2 in the hydrogels were fixed at 2 wt%, 0.1 wt%, and 0.05 wt%, respectively.

Measurements of particle size distribution

The hydrodynamic diameters of CHI-G, CeO_2, and CHI-G/CeO_2 complexes in DDW were measured using a particle size analyzer (SZ-100Z2, Z-202405134881, Horiba, Kyoto, Japan) at the Core Facility for Supporting Analysis & Imaging of Biomedical Materials, Wonkwang University, supported by the National Research Facilities and Equipment Center (NFEC). Briefly, CHI-G (1 mg) was dissolved in DDW (900 μL), and 100 μL of CeO_2 (0.5 mg mL^{-1}) was added to the CHI-G solution to prepare the CHI-G/CeO_2 complex. The particle size distributions of CHI-G (1 mg mL^{-1}), CeO_2 (0.05 mg mL^{-1}), and CHI-G (1 mg mL^{-1})/CeO_2 (0.05 mg mL^{-1}) were measured. In addition, the zeta potentials of all samples were measured under the same experimental conditions. All measurements were performed in triplicate.

Morphological analysis of CHI-G/CeO_2/Gp hydrogels

The morphology and elemental composition of CHI-G/CeO_2/Gp hydrogels were analyzed using scanning electron microscopy equipped with energy-dispersive spectroscopy (SEM-EDS; S-4800, Z-202201147255; Hitachi Ltd, Tokyo, Japan) at the Core Facility for Supporting Analysis and Imaging of Biomedical Materials, Wonkwang University, supported by the National Research Facilities and Equipment Center (NFEC). CHI-G/CeO_2/Gp hydrogels were prepared as described above and subsequently lyophilized. After complete dehydration, the lyophilized samples were sputter-coated with platinum prior to SEM observation. Surface morphologies were examined by SEM, and the elemental distribution of CeO_2 NPs within the hydrogels was evaluated by EDS analysis. CHI-G hydrogels without CeO_2 NPs were used as control samples.

Rheological analysis

The viscoelastic properties of CHI-G/CeO_2/Gp hydrogels were analyzed using a rotational rheometer (Kinexus Lab+, Netzsch, Germany) equipped with a 20 mm parallel plate geometry. For the frequency sweep measurements, the elastic modulus (G') and viscous modulus (G'') were monitored as a function of frequency (0.1 to 10 Hz). In addition, the G' and G'' values of CHI-G/CeO_2/Gp hydrogels before and after addition of genipin were monitored at a predetermined time interval. For the time sweep measurements, a mixture solution of CHI-G (2 wt%, 160 μL) and CeO_2 (20 μL) was placed on the rheometer plate, followed by the addition of 20 μL of genipin. The frequency was

fixed at 1 Hz, and the time point of genipin addition was defined as $t = 0$ s. The dynamic viscoelastic moduli were measured as a function of time. The gelation time was determined from the crossover point of the G' and G''. CHI-G solution without genipin and CeO_2 NPs were used as control samples. All rheological measurements were performed in triplicate.

Measurements of swelling ratios and relative remaining weights

The swelling behavior and relative remaining weights of the CHI-G/CeO_2/Gp hydrogel patches were evaluated in pH 7.4 PBS solutions. To measure the equilibrium swelling ratios, hydrogel patches (approximately 20 mg) were immersed in PBS (1 mL) and incubated at 37 °C for 24 h. After incubation, the swollen patches were gently blotted with filter paper to remove excess surface water, and the wet weights of patches were recorded. The swelling ratio was calculated using the following equation:

$$\text{Swelling ratio}(\%) = \frac{W_{\text{wet}} - W_{\text{dry}}}{W_{\text{dry}}} \times 100\%$$

where $W_{\text{wet}}$and W_{dry} represent the weights of the swollen and dry patches, respectively.

For *in vitro* stability analysis, CHI-G/CeO_2/Gp hydrogel patches (approximately 20 mg) were immersed in PBS (1 mL) and incubated at 37 °C as a function of time. At predetermined time intervals (1, 3, 5, 15, and 30 min; 1, 3, 6, 12, and 24 h; and 3, 5, 7, 14, and 21 days), the patches were collected, rinsed with distilled and deionized water (DDW), and lyophilized. CHI-G hydrogel patches without genipin and CeO_2 NPs were used as control samples. After complete drying, the remaining weight (W_t) was measured, and the relative remaining weight was calculated using the following equation:

$$\text{Remaining weight}\ (\%) = W_t/W_{\text{dry}} \times 100\%$$

All measurements were performed in triplicate.

DPPH radical scavenging assay

The radical scavenging activity of the CHI-G/CeO_2/Gp hydrogel patches was evaluated using a 2,2-diphenyl-1-picrylhydrazyl (DPPH) radical scavenging assay, following the manufacturer's protocol of a commercial DPPH antioxidant assay kit (OxiTec™ DPPH Antioxidant Assay Kit, BIOMAX). DPPH working solution and Trolox standard solutions were prepared according to the supplied instructions. Briefly, the hydrogel patches (20 mg) were placed in assay buffer (400 μL), and DPPH working solution (500 μL) was added to assay buffer, subsequently. The reaction mixtures were incubated at room temperature in the dark for 30 min, and the insoluble patches were carefully removed. The reaction solutions (200 μL) were added on the 96-well plate, and the absorbance at 517 nm was measured using a microplate reader. Trolox standard solutions were used to generate a calibration curve, and appropriate blank wells were prepared to correct background absorbance. The DPPH radical scavenging activity (%) was calculated based on the reduction in absorbance relative to the control using the following equation:

$$\text{DPPH radical scavenging activity}(\%) = \frac{A_{\text{cs}} - A_{\text{s}}}{A_{\text{cs}}} \times 100\%$$

where A_{cs} and A_{s} are the sample and the negative control absorbance at 517 nm. All measurements were performed in triplicate.

Study on tissue adhesive properties

The tissue adhesive properties of the CHI-G/CeO_2/Gp patches were evaluated using a modified lap-shear test with fresh porcine intestine tissues (Bucknam Butcher's Shop, Republic of Korea) and a universal testing machine (UTM, SFM-100 kN, United Calibration, India) equipped with a 50 N load cell. Porcine intestine tissues were cut into square specimens (1 × 1 cm^2) and fixed to the edges of polyethylene terephthalate (PET) films (1 × 5 cm^2) using a commercially available cyanoacrylate adhesive. For adhesion testing, two tissue specimens were overlapped with an effective contact area of 1 × 1 cm^2. Prior to patch application, a thin layer of CHI-G solution was applied to one surface of the patch to serve as an interfacial adhesive layer. The gel-coated side of the patch was then placed between the overlapped porcine intestinal tissues, and gentle pressure was applied to promote intimate contact at the tissue–patch interface. After a short stabilization period, tensile strength was measured by pulling the UTM probe at a constant crosshead speed of 1 mm min^{-1} until failure. CHI-G patches without additional components were used as control samples. All measurements were performed in triplicate.

In vitro bursting pressure measurements

The bursting pressure of the patches was measured using bursting-pressure monitoring devices equipped with a plastic container, indicator, pressure transmitter, and recorder. Fresh porcine intestines were placed in the containers and perforated using a 3 mm biopsy punch and an 18-gauge needle. The patches were cut into a circular shape with a diameter of 10 mm. Prior to application, a thin layer of CHI-G solution was applied to one surface of the patch to serve as an interfacial adhesive. The gel-coated side of the patch was then attached to the perforation site of the intestine, and gentle pressure was applied to ensure intimate contact between the patch and the tissue. Air was subsequently blown into the container, and the internal pressure was continuously monitored. The bursting pressure was determined at the point where a sudden decrease in pressure occurred due to air leakage from the intestine. CHI-G patches without additional components were used as control samples. All measurements were performed in triplicate.

Adhesive strength of the DL-JPatch to multiple tissue

The adhesive strengths of the DL-JPatch and the commercial TA gel (Oramedi™) were assessed using a universal testing machine (TXA™ Standard Texture Analyzer; Yeonjin, Republic of Korea). Fresh porcine oral mucosa purchased from a local

abattoir (Seoul, Republic of Korea) was sectioned into 1 cm × 1 cm squares and gently washed with PBS to remove debris and maintain tissue hydration. The two tissue pieces were overlapped, and the hydrogel patches (CHI-G/TA, CHI-G/CeO_2/Gp) and CTA gel (commercial TA gel) were applied between tissue pieces. The tensile force was calculated by evaluating the strength applied at a crosshead speed of 1 mm sec until separation occurred. The maximum loading force measured was defined as the adhesion strength of hydrogel patches and CTA gel.

Ex vivo mucosal adhesion stability of DL-JPatch

Ex vivo mucosal adhesion was investigated using fresh porcine tongues, purchased from a local market (Seoul, Republic of Korea) to mimic oral conditions. The tongue was positioned at a 45° incline on a custom-made holder, then SL-Patch or DL-JPatch was applied to the mucosal surface of tongue. Artificial saliva (Artificial Saliva for Medical and Dental Research; TMABIO, Republic of Korea) was applied at a flow rate of 5 mL min^{-1} controlled by a syringe pump (Harvard Apparatus, USA) connected to 30 mL syringes. Patch adhesion was recorded until detachment from the tongue by visual observation and digital imaging.

Evaluation of barrier function against bacterial penetration

The protective performance of the patches on irregular surfaces was examined using a transwell system (8 μm pore size; Corning, USA). To simulate an ulcer-like, uneven mucosal surface, the SL-Patch or DL-JPatch was positioned between the upper and lower wells, enabling evaluation of adhesion and sealing capability under irregular interface conditions. An *E. coli* suspension was added to the upper chamber and incubated at 37 °C for 2 h. Bacterial penetration across the patch barrier was assessed by measuring bacterial growth in the lower chamber *via* optical density at 600 nm using a microplate reader.

Cytotoxicity assays

Human gingival fibroblasts (HGF-1) were purchased from ATCC (Manassas, USA). The cells were cultured in culture media (DMEM supplemented with 10% FBS, and 1% antibiotic/antimycotic). For experimental assays, cells were seeded into 24-well plates at a density 3×10^4 cells per well. After incubating for 24 hours, cells were co-cultured with either CHI-G or CHI-G/CeO_2/Gp hydrogel patch, or without a patch, in a transwell system for 24 hours. The viability of co-cultured cells was assessed using Cell Counting Kit-8 (CCK-8; Dojindo Laboratory, Japan) kits and Calcein AM/PI staining. Calcein AM (Thermo Fisher Scientific, USA, C3100MP) stained the live cells and propidium iodide (PI; Sigma Aldrich, USA, P4864) visualized dead cells by fluorescence images.

Evaluation of oral ulcer healing efficacy in an established model

Oral ulcer models were established to evaluate the therapeutic efficacy of the DL-JPatch in difficult-to-heal ulcers. Ulcers were induced on the tongues of male ICR mice (8 weeks old). Briefly, a circular filter paper (1.5 mm in diameter) soaked in 90% acetic acid was placed on the dorsal surface of the tongue for 5 min. This procedure was performed once daily for two consecutive days to reproducibly generate well-defined ulcerative lesions surrounded by intact mucosa. On the following two days, hydrogel patches (blank patch, DL-JPatch, or CTA gel) were carefully applied to the oral mucosal ulcers once daily. For macroscopic imaging of tongue wounds, mice were briefly anesthetized *via* inhalation, and the tongue was gently exteriorized using a custom-designed 3D-printed mouth opener to allow full visualization of the dorsal surface. Control animals without treatment underwent identical anesthesia and handling procedures without patch application. Gross images of the lesions were acquired up to 3 days after the initial patch application to monitor wound closure, which was quantitatively assessed based on lesion area. On the subsequent day, mice were euthanized, and tongue tissues were harvested for histological and immunohistochemical analyses, including hematoxylin and eosin (H&E) staining. Wound closure on day X was calculated by measuring the wound area using ImageJ and normalizing it to the wound area on day 0. Wound closure was expressed as follows;

$$\text{Wound closure rate}_{\text{day } X}(\%) = \frac{(\text{Wound area}_{\text{day 0}} - \text{Wound area}_{\text{day } X})}{\text{Wound area}_{\text{day 0}}} \times 100\%$$

Histological assessment of oral mucosal ulcer healing

For histologic evaluation, fixed tongues were embedded in paraffin and sectioned. Tongue sections were deparaffinized in xylene, followed by stepwise rehydration in decreasing concentrations of ethanol. Heat-induced antigen retrieval was performed in 0.01 M citrate buffer (pH 6.0) using microwave treatment. Endogenous peroxidase activity was blocked by incubation with a peroxidase-blocking solution (DAKO, Agilent, USA). The sections were then incubated for 30 min with primary antibodies against CK13, CD11b, and 4HNE (1 : 200 dilution; Abcam, UK). After washing, antibody binding was visualized by incubation with an HRP-labeled anti-rabbit polymer secondary reagent from the EnVision+ System (DAKO, Agilent, USA) for 30 min. Color development was achieved using DAB substrate (DAKO, Agilent, CA, USA), and nuclear counterstaining was performed with Mayer's hematoxylin. The stained sections were subsequently dehydrated, cleared, coverslipped, and digitized at 400× magnification using an Aperio AT2 slide scanner (Leica, Germany). For histological scoring system integrating therapeutic outcomes, the percentage of positively stained area (CK13, CD11b, NF-κB, and 4HNE) was measured and categorized into five graded ranges (Score 0–4) based on the distribution of values across all samples (Table S1). An integrated histological score was calculated by summing the individual scores of each marker to provide an overall assessment of tissue recovery.

In vivo biosafety assessment

For short-term systemic safety assessment, DL-JPatch was applied to a large ulcerated region of the tongue for two

consecutive days (one patch per day). Seven days after the final application, major organs including the spleen, kidney, liver, and heart were collected and processed for quantitative determination of cerium content using ICP-MS. Histopathological evaluation was performed in a separate cohort of mice in which DL-JPatch was applied to the healthy tongue following the same application schedule. Seven days after the final application, the tongue and major organs – including the spleen, duodenum, kidney, liver, heart, and stomach – were collected, fixed in 4% paraformaldehyde for 2 days, embedded in paraffin, sectioned, and stained with hematoxylin and eosin (H&E). Body weight was monitored for 3 weeks following the first DL-JPatch application to assess long-term *in vivo* safety. During this period, the patch was applied four times (on days 1, 2, 7, and 14).

Animal care and ethical approval

All animal experiments were conducted in accordance with the guidelines and protocols approved by the Institutional Animal Care and Use Committee (IACUC) of the Seoul National University College of Medicine (Approval number: SNU-251023-5). Male ICR mice (8 weeks old) were housed under conventional conditions with controlled temperature (22 ± 2 °C), humidity (50–60%), and a 12-hours light/dark cycle, with free access to standard chow and water.

Statistical analysis

All quantitative results are reported as mean values with corresponding standard deviations (SD). Group differences were evaluated by applying one-way ANOVA followed by Tukey's multiple-comparison procedure, or by Student's *t*-test when applicable, using Prism 10 (GraphPad Software). Statistical significance was defined according to *p*-values obtained from comparisons with the control group. The presented data represent typical outcomes from experiments independently performed at least three times, each yielding comparable results. The sample size (n) refers to the number of independent biological replicates included in each group.

Results and discussion

Synthesis and preparations of CHI-G/CeO_2/Gp hydrogels

CHI-G was synthesized *via* carbodiimide-mediated coupling between the primary amine groups of chitosan and the carboxylic acid groups of gallic acid, forming amide linkages as schematically illustrated in Fig. 1a. The conjugation of gallic acid to chitosan was confirmed by both ^{1}H NMR and UV-Vis spectroscopic studies (Fig. 1b and c). As shown in Fig. 1b, the ^{1}H NMR spectrum of CHI-G exhibited characteristic aromatic proton signals attributed to the gallol groups, observed in the range of approximately 6.8–7.2 ppm, which is consistent with previously reported gallic acid-conjugated chitosan.[26–28] UV-Vis spectroscopic analysis further supported gallic acid conjugation. As shown in Fig. 1c, CHI-G showed a distinct absorbance peak around 265 nm, corresponding to the π–π* transitions of the aromatic gallol groups. The degree of gallic acid substitution (DS) in CHI-G were 3.7 and 7.5%, respectively, as determined by UV-Vis spectroscopic analysis.

CHI-G/CeO_2/Gp hydrogels were prepared by genipin-mediated crosslinking of CHI-G in the presence of CeO_2 NPs, followed by lyophilization to obtain the hydrogel patches. As illustrated in Fig. 1d, a CeO_2 NP-dispersed solution (100 μL) and a genipin solution (100 μL) were sequentially added to the CHI-G solution. The mixture of CHI-G, CeO_2 NPs, and genipin was incubated at 37 °C for 1 h to induce the gelation through genipin-mediated crosslinking. As previously reported, the genipin reacts with the primary amine groups of chitosan backbone to form the chitosan-based hydrogels.[29–31] After crosslinking, the hydrogels were lyophilized to prepare the CHI-G/CeO_2/Gp hydrogel patches. As shown in Fig. 1e, the CHI-G alone was flowed downward in the vial-inverting tests, whereas CHI-G immediately after the addition of genipin showed no flow, indicating rapid gelation. In addition, the color of both CHI-G/Gp and CHI-G/CeO_2/Gp hydrogels changed upon genipin-mediated crosslinking. As previously reported, genipin-crosslinked chitosan hydrogels exhibit a blue to dark-blue coloration due to the formation of chitosan–genipin linkages.[32] Distinct differences in the UV-Vis spectra of CHI-G before and after genipin addition were observed. As shown in Fig. 1f, CHI-G after genipin addition exhibited broadened absorption in the 200–400 nm wavelength range. In addition, the baseline of the UV-Vis spectra of both CHI-G/Gp and CHI-G/CeO_2/Gp solutions was upshifted, indicating that insoluble aggregates were generated by CHI-G crosslinking (Fig. 1f). Interestingly, the CeO_2 NP-dispersed solution alone showed an overall baseline upshift across all wavelengths, whereas the CHI-G/CeO_2/Gp solution immediately after genipin addition did not show such an upshift. The particle size distribution of the CHI-G/CeO_2 supported enhanced dispersibility of CeO_2 in CHI-G polymeric networks. As shown in Fig. 1g, the particle size of CHI-G without any additives was 0.83 to 1.97 μm. The CeO_2 NP without any treatments showed significant aggregations in aqueous solution (Fig. 1h). However, the particle sizes of CHI-G and CeO_2 mixtures were 315.27 to 454.69 nm, indicating that the CHI-G networks affected the dispersion of CeO_2 (Fig. 1i). In addition, zeta potential values of CHI-G, CeO_2, and CHI-G/CeO_2 were 3.37 ± 0.39, −0.33 ± 0.26, and 2.77 ± 0.21 mV, respectively (Fig. 1j). This observation suggests that CHI-G contributes to maintaining the dispersibility of CeO_2 NPs. The morphological studies of CHI-G/CeO_2/Gp hydrogel patches also supported the formation of CHI-G/CeO_2/Gp structures. Fig. 1k presents the lyophilized CHI-G structures without addition of CeO_2 NPs or genipin. After addition of Gp, the CHI-G/Gp hydrogel patches showed a relatively denser structure due to the crosslinking (Fig. 1l). Upon incorporation of CeO_2 NPs, CHI-G/CeO_2/Gp hydrogel patches displayed microstructures similar to those of CHI-G/Gp hydrogels (Fig. 1m). In addition, enlarged SEM images with corresponding EDS spectra confirmed that CeO_2 NPs were embedded within the CHI-G network (Fig. 1n).

Characterizations of CHI-G/CeO_2/Gp hydrogels

The gelation behaviors and viscoelastic properties of CHI-G/CeO_2/Gp hydrogels were monitored using a rotational

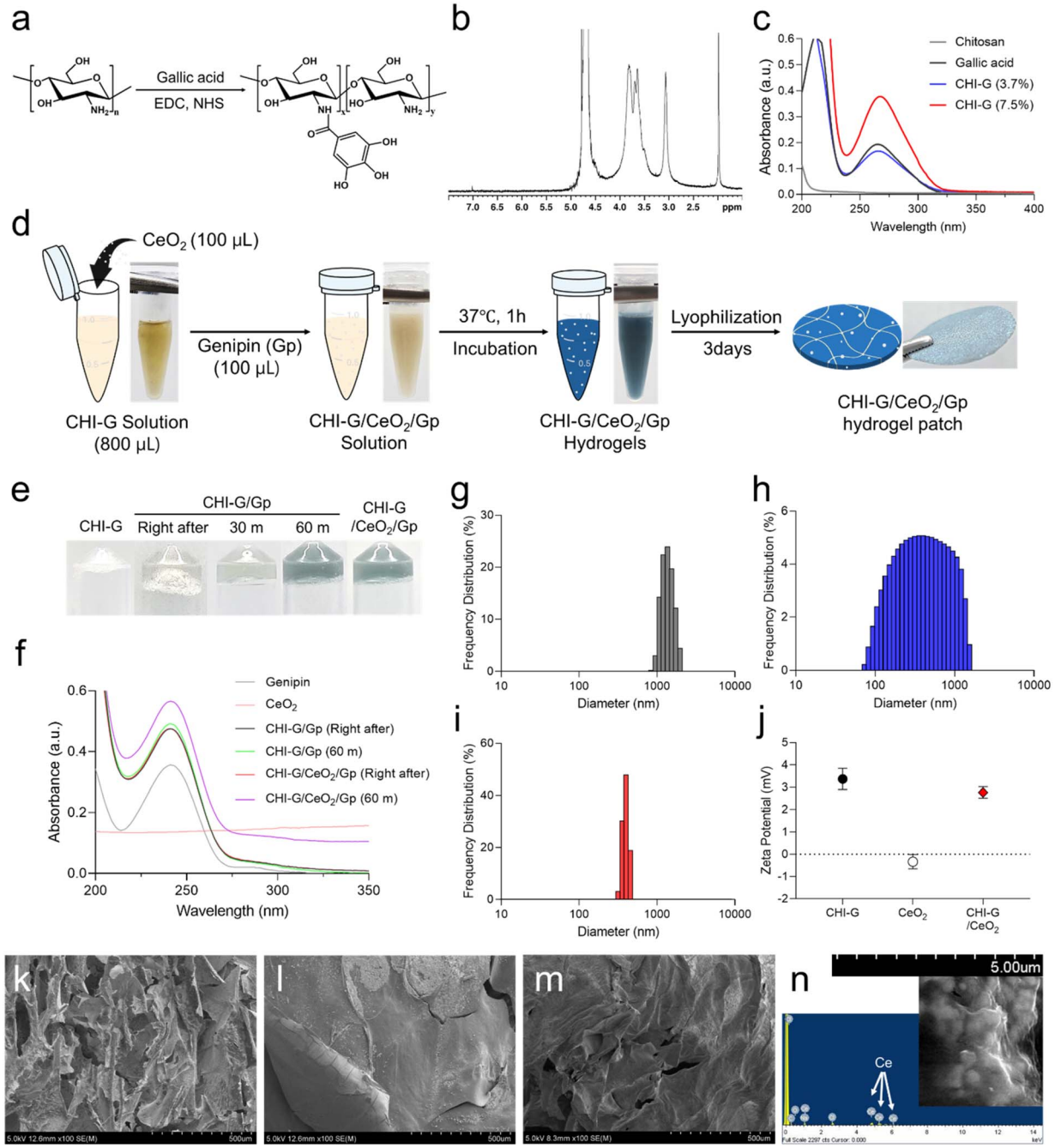

Fig. 1 (a) Synthesis and chemical structures of CHI-G. (b) ^{1}H NMR spectrum of CHI-G. (c) UV-Vis spectra of chitosan, gallic acid, and CHI-G (DS = 3.7 and 7.5%). (d) Schematic illustration and photographic images of the preparation of the CHI-G/CeO_2/Gp hydrogel patches. (e) Photographic images of CHI-G, CHI-G right after addition of Gp, CHI-G/Gp hydrogels after 30 m-incubation, CHI-G/Gp hydrogels after 60 m-incubation, and the CHI-G/CeO_2/Gp hydrogels after 60 m-incubation. (f) UV-Vis spectra of genipin, CeO_2 NPs, and CHI-G and CHI-G/CeO_2 solutions after addition genipin. (g–i) Particle size distributions of CHI-G (g), CeO_2 (h), CHI-G/CeO_2 complexes (i). (j) Zeta potential of CHI-G, CeO_2, and CHI-G/CeO_2 complexes. (k–n) SEM images of CHI-G (k), CHI-G/Gp (l), and CHI-G/CeO_2/Gp (m) hydrogel patches. (n) enlarged view of SEM images with EDS spectrum of the CHI-G/CeO_2/Gp hydrogel patches.

rheometer. The CHI-G solution alone showed no gelation behavior (Fig. 2a). However, the CHI-G/Gp (Fig. 2b) and CHI-G/CeO_2/Gp hydrogels (Fig. 2c) after 60 min incubation exhibited higher elastic (G') moduli than viscous (G'') moduli, indicating the formation of stable hydrogels. No significant increase in G' values was observed for CHI-G/CeO_2/Gp hydrogels compared to CHI-G/Gp hydrogels without CeO_2 NPs, which may be attributed to the low concentration of CeO_2 NPs. In addition, the gelation times of CHI-G/CeO_2/Gp hydrogels prepared from CHI-G with DS values of 3.7 and 7.5% were monitored using time sweep measurements. As shown in Fig. S1a, the gelation times of CHI-G/CeO_2/Gp hydrogels prepared from CHI-G with DS values of

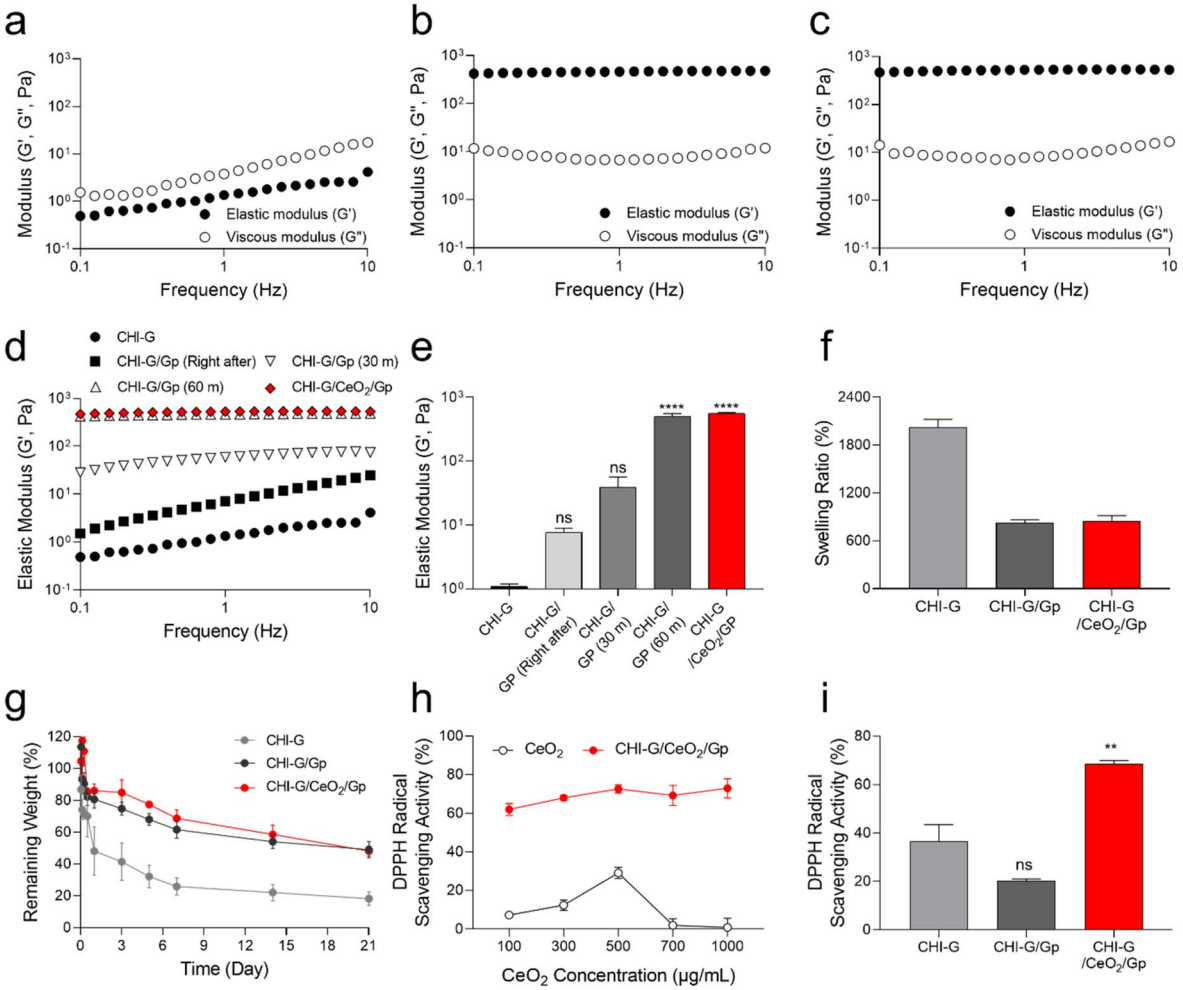

Fig. 2 (a–c) Frequency sweep measurements of CHI-G (a), CHI-G/Gp hydrogels after 60 m-incubation (b), and CHI-G/CeO_2/Gp hydrogels after 60 m-incubation (c). (d) Elastic modulus (G') value changes of CHI-G/Gp and CHI-G/CeO_2/Gp hydrogels after addition of Gp as a function of incubation time. (e) Average elastic modulus (G') values of CHI-G, CHI-G right after addition of Gp, CHI-G/Gp hydrogels after 30 m-incubation, CHI-G/Gp hydrogels after 60 m-incubation, and the CHI-G/CeO_2/Gp hydrogels after 60 m-incubation. ($n = 3$, ns: no significance, ****$p <$ 0.0001, one-way ANOVA test) (f) equilibrium swelling ratios and (g) relative remaining weights of CHI-G, CHI-G/Gp, and CHI-G/CeO_2/Gp hydrogels. (h) DPPH radical scavenging activities of CeO_2 NPs and CHI-G/CeO_2/Gp hydrogels as a function of CeO_2 concentrations. (i) DPPH radical scavenging activities of CHI-G, CHI-G/Gp, and CHI-G/CeO_2/Gp hydrogels at a concentration of 500 μg mL^{-1} CeO_2. ($n = 3$, ns: no significance, **$p < 0.01$, one-way ANOVA test).

3.7 and 7.5% were 195 and 30 s. In addition, the G' value of CHI-G/CeO_2/Gp hydrogels prepared from CHI-G with 7.5% DS was higher than that of CHI-G/CeO_2/Gp hydrogels prepared from CHI-G with 3.7% DS across the measured frequency range (Fig. S1b). Based on the faster gelation and improved elastic moduli, CHI-G with a DS of 7.5% was used for the preparation of CHI-G/CeO_2/Gp hydrogels in subsequent experiments. Furthermore, the G' values of CHI-G/Gp hydrogels were monitored as a function of time (Fig. 2d). The G' values were 1.10 ± 0.07 Pa for CHI-G, 7.74 ± 0.88 Pa for CHI-G/Gp (immediately after genipin addition), 38.82 ± 14.0 Pa for CHI-G/Gp (30 min), and 501.67 ± 43.63 Pa for CHI-G/Gp (60 min) hydrogels, respectively. The G' values of the CHI-G/CeO_2/Gp hydrogels slightly increased to 556.6 ± 17.95 Pa, but this difference was not statistically significant (Fig. 2e).

The equilibrium swelling ratios of CHI-G/CeO_2/Gp hydrogels were evaluated after incubation in pH 7.4 PBS solution for 24 h (Fig. 2f). The CHI-G patch without the CeO_2 NPs and Gp exhibited a high swelling ratio of 2026.2 ± 77.5%, whereas the swelling ratios of CHI-G/Gp and CHI-G/CeO_2/Gp hydrogel patches were significantly reduced to 829.4 ± 29.6% and 852.4 ± 52.0%, respectively. The reduced swelling ratios of CHI-G with and without CeO_2 NPs after addition of genipin indicated an increased crosslinking density of the hydrogels. The *in vitro* stability of the patches was further evaluated by monitoring their remaining weights in pH 7.4 PBS over time (Fig. 2g). The CHI-G patches showed a rapid decrease in their remaining weight at the early stage, followed by gradual mass loss over 21 days. CHI-G patches without genipin can undergo self-crosslinking over time due to physical interactions (*i.e.*, hydrogen bonds) and

slowly formed chemical crosslinks. The remaining weight of the CHI-G patch was 18.17 ± 3.57% after 21 days. In contrast, CHI-G/Gp and CHI-G/CeO_2/Gp hydrogel patches exhibited improved stability, retaining 49.08 ± 4.15% and 48.12 ± 2.73% of their initial weights after 21 days, respectively. These results indicate that genipin crosslinking effectively suppresses excessive swelling and enhances the structural stability of CHI-G patches under physiological conditions, while CeO_2 incorporation does not compromise these properties.

The radical scavenging activities of CHI-G/CeO_2/Gp hydrogels were monitored using a DPPH assay. The CeO_2 NPs have excellent scavenging capability of superoxide radicals and hydrogen peroxide, as previously reported.[20] However, the CeO_2 NPs in this study exhibited a non-monotonic concentration response with diminished activity at higher concentrations (Fig. 2h). Although hydrothermally synthesized CeO_2 NPs possesses redox-active surface sites, its apparent radical-scavenging performance in solution was limited, likely due to concentration-dependent aggregation and sedimentation that reduce the accessible surface area and hinder interfacial contact with radicals.[33] In contrast, incorporation of CeO_2 NPs into the genipin-crosslinked CHI-G network maintained high scavenging activity across concentrations, which we attribute to matrix-mediated dispersion and immobilization that suppresses particle–particle aggregation and preserves reactive surface exposure (Fig. 2h). The radical scavenging activity of CHI-G/CeO_2/Gp hydrogels reached 68.6 ± 1.3%, which was significantly higher than that of CHI-G patches without genipin and CeO_2 NPs (36.7 ± 6.8%) and genipin-crosslinked CHI-G patches without CeO_2 NPs (20.2 ± 0.8%) (Fig. 2i). These results suggest that the genipin-crosslinked CHI-G network enhances CeO_2 NP dispersion, thereby improving radical scavenging performance.

Tissue adhesiveness and bursting pressure of CHI-G/CeO_2/Gp hydrogels

Tissue adhesive properties of CHI-G/CeO_2/Gp hydrogel patches were evaluated using porcine intestinal tissues. The

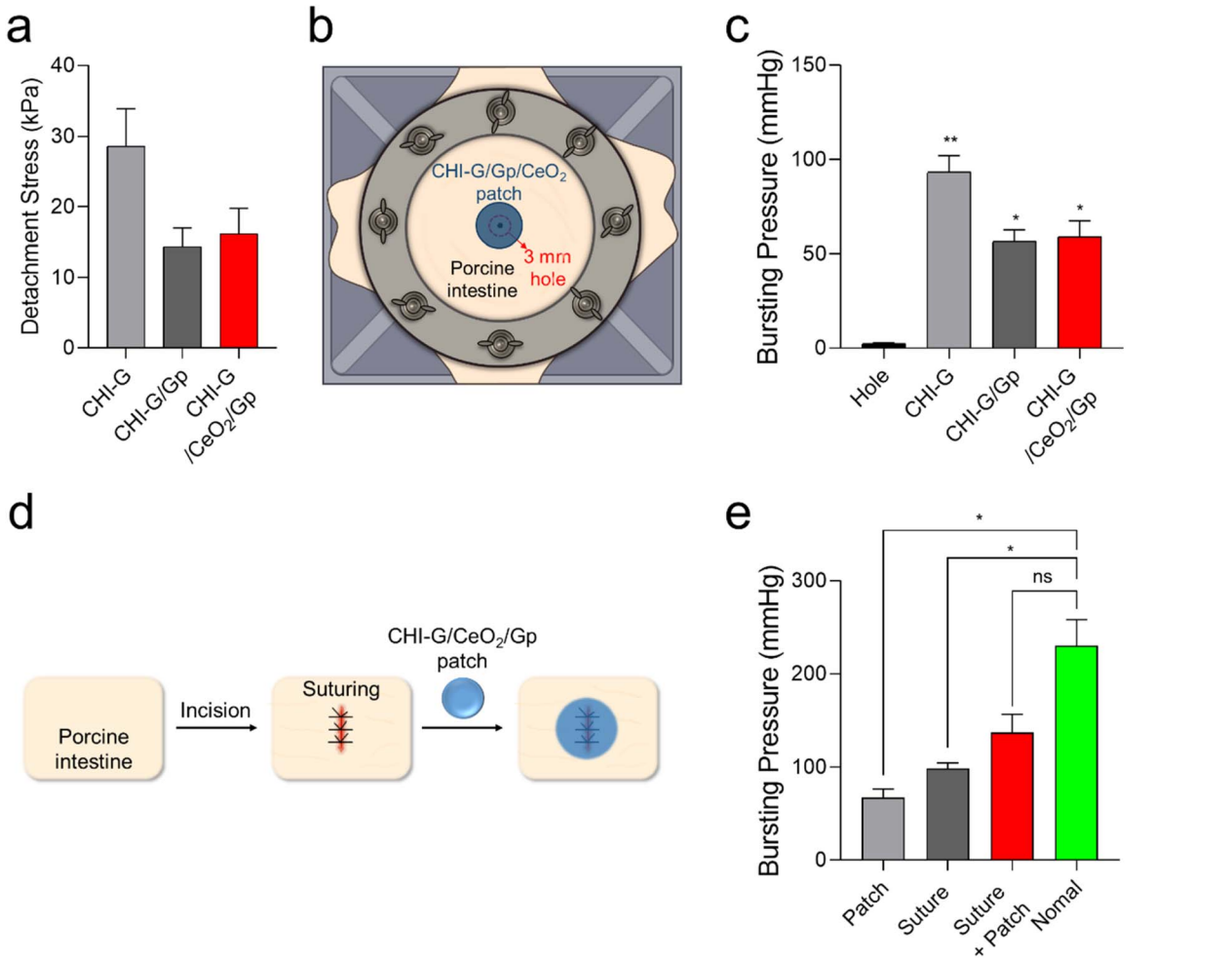

Fig. 3 (a) Detachment stresses of CHI-G, CHI-G/Gp, and CHI-G/CeO_2/Gp hydrogel patches. (b) Schematic illustrations of bursting pressure measurement of intestine tissues with 3 mm. (c) bursting pressures of CHI-G, CHI-G/Gp, and CHI-G/CeO_2/Gp hydrogel patches. ($n = 3$, *p < 0.05, **p < 0.01, one-way ANOVA test) (d) schematic illustrations of bursting pressure measurement of intestine tissues with 10 mm-long incision and suturing with patches. (e) Measured bursting pressures of incision after applying patch, after suturing, after suturing with patches, and normal intestine tissues. ($n = 3$, ns: no significance, *p < 0.05, one-way ANOVA test).

detachment stresses were measured by pulling the UTM probe after the two porcine intestines were attached using CHI-G/CeO_2/Gp hydrogel patches. As shown in Fig. 3a, the detachment stress of CHI-G hydrogel patches was 28.6 ± 5.32 kPa. After genipin crosslinking, the detachment stresses of CHI-G/Gp and CHI-G/CeO_2/Gp hydrogel patches decreased to 14.37 ± 2.63 kPa and 16.13 ± 3.64 kPa. This reduction is likely attributable to consumption of free amine groups during crosslinking and increased structural rigidity of both CHI-G/Gp and CHI-G/CeO_2/Gp hydrogel patches. In addition, the sealing performance of CHI-G/CeO_2/Gp hydrogel patches was further evaluated by measuring bursting pressures using porcine intestinal tissues. As illustrated Fig. 3b, CHI-G/CeO_2/Gp hydrogel patches were applied to pre-formed perforation sites on the intestine. After that, air was supplied until a sudden decrease in pressure was observed. As shown in Fig. 3c, the pressure of the intestine with a hole was 2.43 ± 0.26 mmHg. After sealing the hole with CHI-G hydrogel patches, the bursting pressure increased to 93.32 ± 7.14 mmHg. In addition, the CHI-G/Gp and CHI-G/CeO_2/Gp hydrogel patches showed bursting pressures of 56.61 ± 4.94 mmHg and 59.08 ± 6.80 mmHg, respectively. To closely evaluate the sealing behavior under more clinically relevant conditions, bursting pressure measurements were conducted using sutured intestinal tissues (Fig. 3d). The bursting pressure of the intestine sealed with a CHI-G/CeO_2/Gp hydrogel patch after suturing was 137.45 ± 15.68 mmHg, which was significantly higher than that of the sutured intestine alone (98.98 ± 4.60 mmHg) (Fig. 3e). Although the bursting pressure of CHI-G/CeO_2/Gp hydrogel patches remained lower than that of intact intestinal tissue (230.28 ± 22.95 mmHg), these results demonstrate the strong sealing capability and translational potential of CHI-G/CeO_2/Gp hydrogel patches for soft-tissue applications.

Designing optimized dual-layered Janus patch for oral application

The oral cavity presents a uniquely challenging environment for localized therapeutic delivery due to constant salivary flow, complex mucosal topography, and repetitive mechanical stresses generated by tongue movement and swallowing. To address these challenges, we designed a dual-layered Janus patch (DL-JPatch) in which each layer is structurally and functionally optimized for a distinct role: a tissue-adaptive, highly adhesive CHI-G/TA layer facing the ulcer bed, and a genipin-crosslinked, CeO_2-containing CHI-G/CeO_2/Gp layer forming a mechanically stable, non-adhesive outer surface.

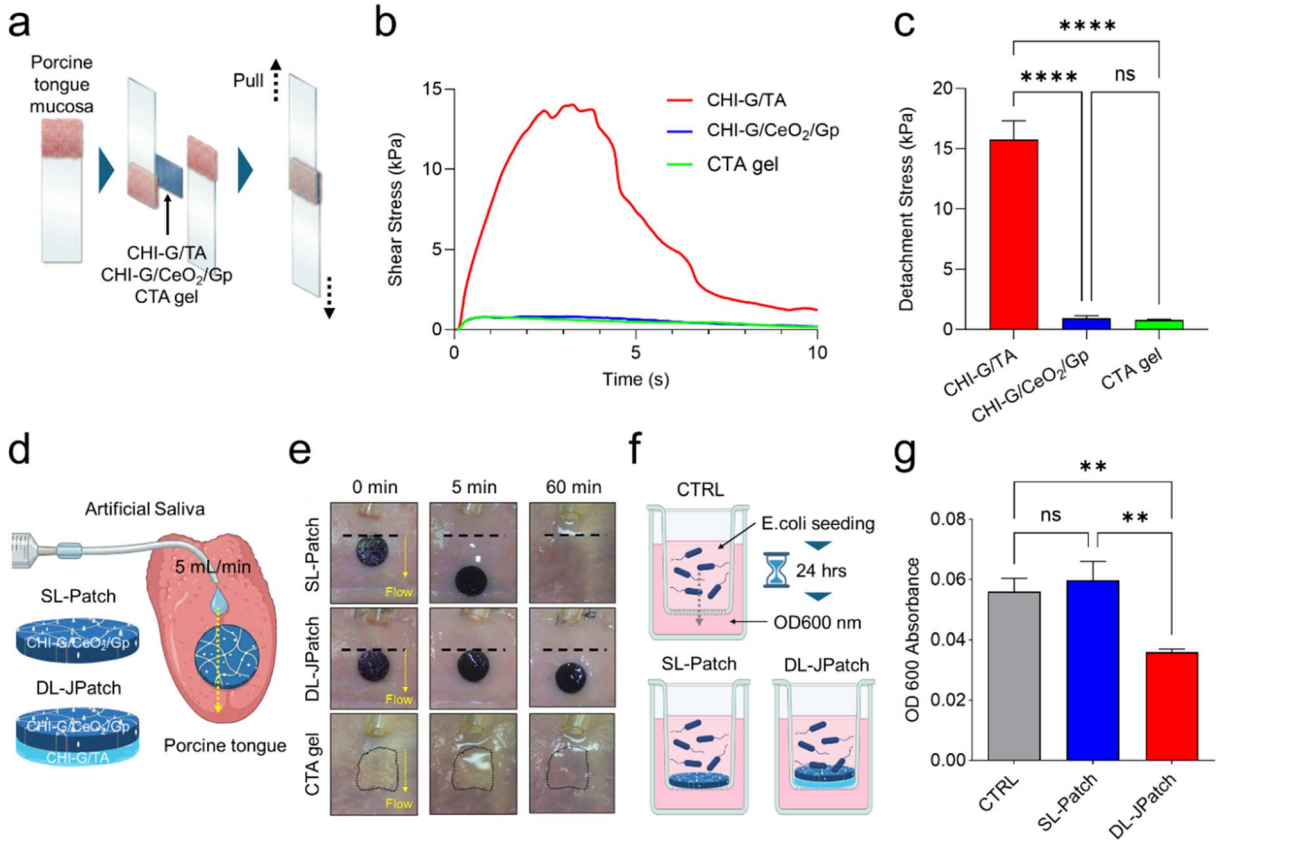

Fig. 4 (a) Schematic illustrations of the lap-shear test on porcine tongue mucosal surfaces. (b) Time-dependent shear stresses of CHI-G/TA, CHI-G/CeO_2/Gp hydrogel patches and CTA gel. (c) Detachment stresses of CHI-G/TA, CHI-G/CeO_2/Gp hydrogel patches and CTA gel. ($n = 3$–4 per group, ns: no significance, ****$p < 0.0001$, one-way ANOVA test) (d and e) Mucosal adhesiveness measurement of SL-Patch, DL-JPatch and CTA gel. (f and g) Bacterial barrier function assay in transwell system ($n = 3$, ns: no significance, **$p < 0.01$, one-way ANOVA test). All data are means ± s.d.

To validate this design rationale, the interfacial adhesive properties of individual layers were first quantitatively compared using a lap-shear test on fresh porcine tongue mucosa (Fig. 4a). The CHI-G/TA layer exhibited a significantly higher detachment stress than both the CHI-G/CeO_2/Gp layer and a commercial triamcinolone acetonide (CTA) gel control (Fig. 4b and c). These results highlight the critical role of free gallol groups in CHI-G/TA, which enable strong wet-tissue adhesion through multivalent hydrogen bonding and catechol-like interactions.[14] In contrast, genipin crosslinking in the CHI-G/CeO_2/Gp layer significantly reduced interfacial adhesion, likely due to consumption of primary amine groups and increased network rigidity. Importantly, the detachment stress of CHI-G/CeO_2/Gp was comparable to that of CTA gel, confirming that the outer layer minimizes nonspecific mucosal adhesion – an essential requirement to reduce discomfort and undesired non-specific attachment in the oral cavity.

Beyond static adhesion strength, resistance to salivary washout was evaluated using an ex vivo porcine tongue model under continuous artificial saliva flow (5 mL min^{-1}), simulating physiologically relevant oral conditions (Fig. 4d). While single-layer (SL) patches composed solely of CHI-G/CeO_2/Gp detached rapidly under flow, the DL-JPatch remained stably anchored to the mucosal surface for at least 60 min (Fig. 4e). Notably, the DL-JPatch maintained its position without lateral displacement or edge-lifting, whereas the CTA gel control was readily disappeared. These results demonstrate that spatial confinement of strong adhesion to the tissue-facing side, rather than uniform bulk adhesiveness, is essential for maintaining patch retention under dynamic oral conditions.

In addition to mechanical retention, the Janus architecture was designed to function as a physical and biological barrier against microbial infiltration. To assess this, a transwell-based bacterial penetration assay was performed using *E. coli* as a model microorganism (Fig. 4f). While no significant reduction in bacterial transmission was observed with the SL patch relative to the untreated control, the DL-JPatch significantly suppressed bacterial passage across the interface, as quantified by absorbance at OD_{600} measurements in the lower chamber (Fig. 4g). This enhanced barrier function is attributed to the conformal sealing provided by the adhesive CHI-G/TA layer in combination with the mechanically stable, crosslinked CHI-G/CeO_2/Gp layer, expected to minimize micro-gaps along irregular mucosal surfaces.

Collectively, these results validate the design logic of the dual-layered Janus architecture simultaneously achieving robust fixation to ulcerated mucosa, resistance to salivary shear forces, minimized nonspecific adhesion, and effective barrier protection against bacterial infiltration.

Biocompatibility of dual-layered Janus patch (DL-JPatch)

The cytotoxicity of individual DL-JPatch components was first evaluated *in vitro* using human gingival fibroblasts (HGF-1). Cells were co-cultured with either the CHI-G/TA layer or the CHI-G/CeO_2/Gp layer for 24 h, as schematically illustrated in Fig. 5a. Live/dead staining revealed that HGF-1 cells maintained a typical elongated, spindle-shaped morphology with strong Calcein-AM fluorescence in both treatment groups, comparable to the untreated control (CTRL) (Fig. 5b). Consistently, no significant increase in propidium iodide (PI)-positive cells was observed following exposure to either layer (Fig. 5b), and quantitative analysis confirmed no statistically significant difference in live/dead cell ratios among the groups (Fig. 5c). Cellular metabolic activity was further assessed using the CCK-8 assay. Both CHI-G/TA and CHI-G/CeO_2/Gp-treated cells exhibited metabolic activity levels comparable to those of the CTRL group, with no statistically significant differences detected (Fig. 5d). These results collectively indicate that neither the adhesive CHI-G/TA layer nor the genipin-crosslinked CHI-G/CeO_2/Gp layer exerts detectable cytotoxic effects on gingival fibroblasts.

To further assess the *in vivo* systemic safety of DL-JPatch, the patch was repeatedly applied to the healthy tongue of the mice on days 1, 2, 7, and 14, while body weight was monitored for 3 weeks. No significant differences in body weight were observed between the DL-JPatch and CTRL groups throughout the monitoring period, indicating the absence of systemic toxicity upon repeated applications (Fig. 5e).

The potential risk of cerium leaching and associated tissue toxicity *in vivo* was also evaluated. DL-JPatch was applied to a large ulcerated region of the tongue for two consecutive days (one patch per day). Seven days after the final application, major organs including spleen, kidney, liver, and heart, were harvested and analyzed by inductively coupled plasma (ICP) spectroscopy. Cerium ions were not detected above the minimum detection limit in any of the examined tissues (Table S2), indicating negligible systemic accumulation. These findings indicate that CeO_2 microparticles are effectively immobilized within the genipin-crosslinked CHI-G matrix, thereby minimizing the risk of particle leaching or systemic distribution.

Finally, to evaluate tissue-level toxicity, histological examination was performed on major organs including the spleen, duodenum, kidney, liver, heart, and stomach one week after patch application. No observable pathological abnormalities were detected in the tongue and major organs following DL-JPatch treatment (Fig. 5f). Taken together, these *in vitro* and *in vivo* assessments demonstrate that DL-JPatch exhibits excellent cytocompatibility and systemic safety. The absence of detectable cerium accumulation in major organs indicates minimal systemic exposure and highlights the structural stability of the genipin-crosslinked CeO_2-containing layer, supporting the suitability of DL-JPatch for localized oral applications requiring prolonged mucosal contact. Nevertheless, a comprehensive preclinical toxicity study incorporating serum biochemistry, hematological profiling, and extended observation periods should be performed prior to clinical translation.

Therapeutic efficacy of DL-JPatch in an oral ulcer model

The therapeutic efficacy of DL-JPatch was evaluated using a chemically induced oral ulcer model in mice, which recapitulates key pathological features of human oral ulcers, including epithelial disruption, inflammatory responses, and oxidative

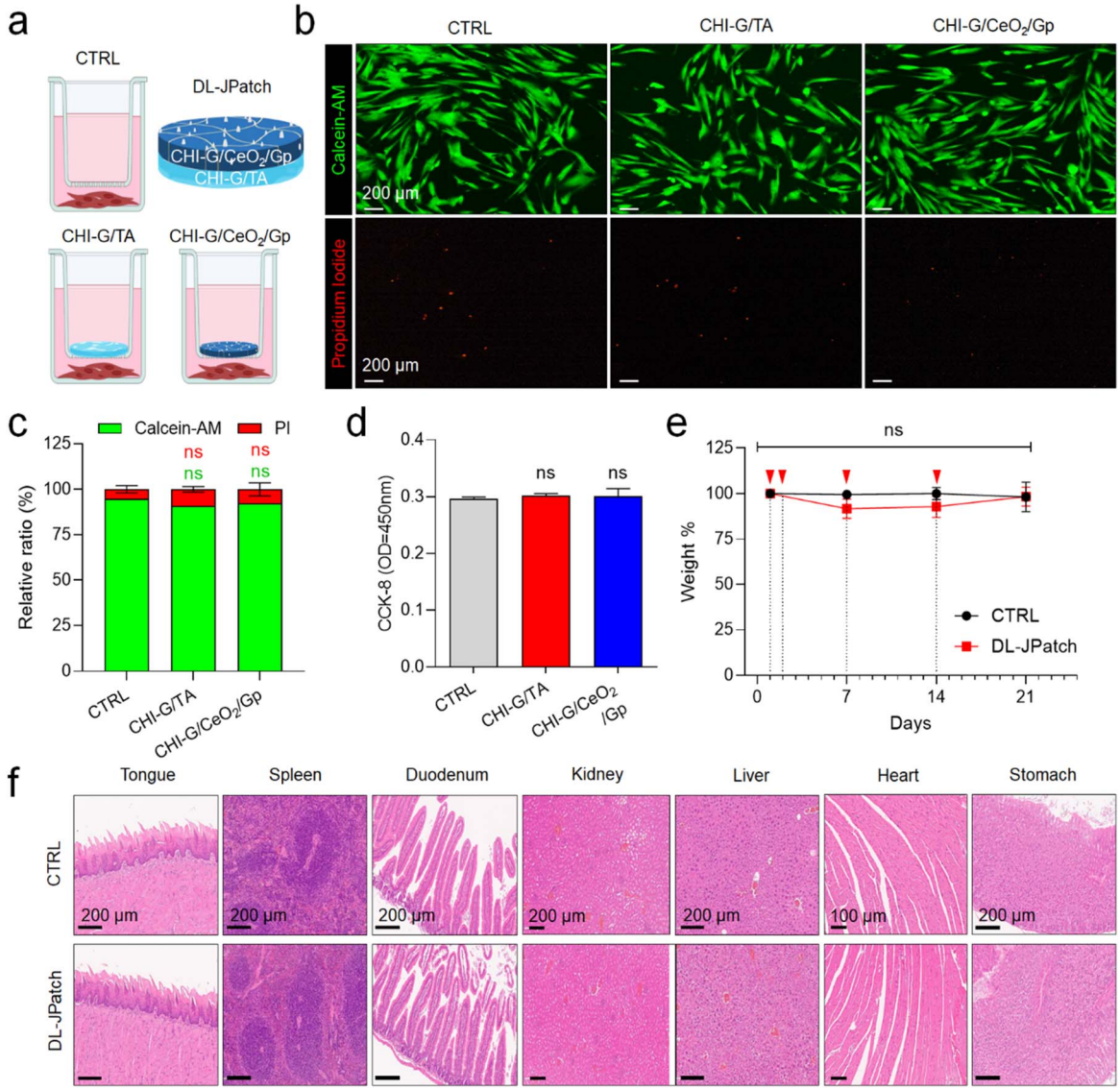

Fig. 5 (a) Experimental setup to evaluate the cytotoxicity of individual DL-JPatch components. (b) Comparison of fluorescence images showing human gingival fibroblasts (HGF-1) labeled with Calcein AM (live, green) or Propidium iodide (dead, red) after 24 h of co-culture with hydrogel patches (blank patch, CHI-G/TA, CHI-G/CeO_2/Gp). (c) Quantification of the relative proportions of live and dead cell populations. ($n = 5$–7 per group, ns: no significance, one-way ANOVA test) (d) cell viability measured by absorbance at 450 nm using CCK-8 assay after 24 h of co-culture with hydrogel patches (blank patch, CHI-G/TA, CHI-G/CeO_2/Gp). ($n = 3$, ns: no significance, one-way ANOVA test) (e) Relative body weight changes over 21 days. Red arrows and dotted lines indicate the days of repetitive patch application (days 1, 2, 7, and 14). ($n = 3$, ns: no significance, two-way ANOVA test). (f) Representative H&E-stained images of each organs isolated 7 days after final application. All data are means ± s.d.

stress.[4] Representative gross images of tongue ulcers acquired over a 3-days treatment period are shown in Fig. 6a. Untreated ulcers (No tx.) exhibited limited spontaneous healing, with persistent ulcer boundaries and irregular wound margins throughout the observation period (Fig. 6a). In contrast, CTA gel, DL-JPatch (-TA), and DL-JPatch treatments promoted visible wound contraction compared with the untreated group. Notably, DL-JPatch resulted in the most rapid and significant reduction in wound area, particularly from Day 2 onward. While DL-JPatch (-TA) and CTA gel groups exhibited a trend toward improved wound closure, the differences were not statistically significant (Fig. 6a–c). To visualize temporal wound closure dynamics, ulcer contours were overlaid across time points (Fig. 6b). The DL-JPatch group demonstrated a more compact and concentric reduction pattern compared to the diffuse and asymmetric closure observed in the other groups suggesting more uniform re-epithelialization (Fig. 6b). Quantitative analysis also confirmed these observations (Fig. 6c). While no statistically significant differences in wound closure were observed among groups at Day 1, DL-JPatch treatment resulted in significantly greater wound closure by Day 2 compared to both CTA gel and DL-JPatch(-TA) groups (Fig. 6c). By Day 3, DL-

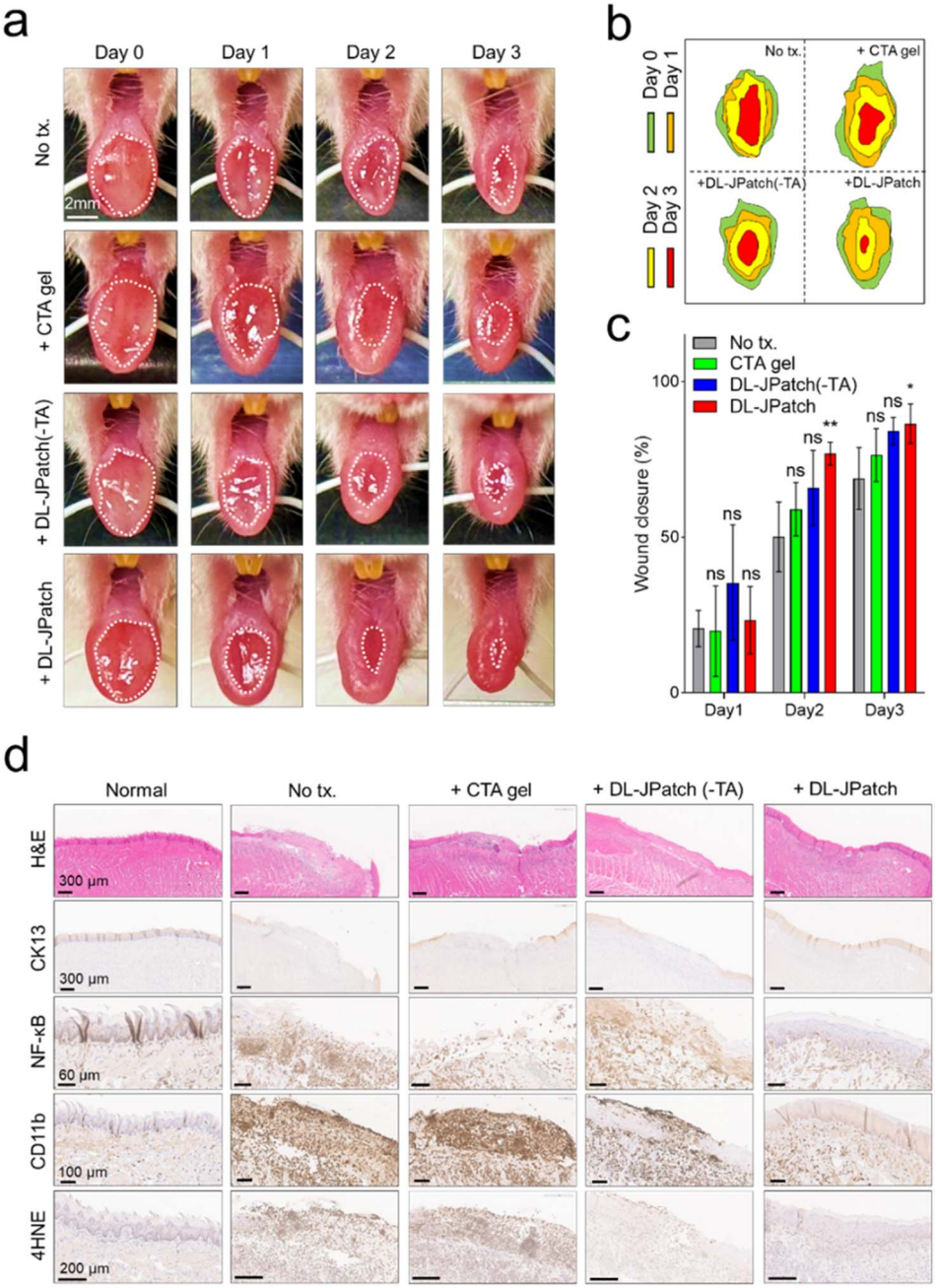

Fig. 6 (a) Representative gross photographs showing progressive regeneration of ulcer in untreated (No tx.: No treat), CTA gel treated DL-JPatch (-TA) and DL-JPatch treated groups. (b) Overlaid ulcer area maps outlining the wound margins across time points. (c) Wound closure rates of the ulcers over time. ($n = 3$–5, ns: no significance, *$p < 0.05$, **$p < 0.01$, one-way ANOVA test) (d) H&E- and Immunohistochemical-stained images of sectioned tongues detecting CK13 (keratinized layer), NF-κB (inflammatory signal), CD11b(leukocyte) and 4HNE (oxidative stress). All data are means ± s.d.

JPatch achieved the highest wound closure, exceeding that of other groups, indicating sustained therapeutic benefit rather than transient suppression of inflammation (Fig. 6c).

Histological evaluation further validated the macroscopic findings (Fig. 6d). Hematoxylin and eosin (H&E) staining revealed incomplete epithelial coverage and persistent inflammatory infiltration in untreated ulcers, whereas CTA gel-and DL-JPatch(-TA)-treated tissues showed partial epithelial regeneration with irregular epithelial thickness (Fig. 6d, first row). Relative to the other groups, DL-JPatch-treated ulcers exhibited more continuous epithelial layers with restored tissue architecture (Fig. 6d, first row). Immunohistochemical staining for cytokeratin 13 (CK13), a marker of differentiated oral epithelium, showed enhanced epithelial maturation in the DL-JPatch group compared to the other groups, approaching the CK13 expression pattern observed in normal tongue

epithelium, supporting accelerated re-epithelialization (Fig. 6d, second row).

The superior therapeutic efficacy of DL-JPatch can be understood within the framework of the ROS-inflammation amplification loop that characterizes the oral ulcer microenvironment. Tissue damage at the ulcer site triggers excessive ROS generation through mitochondrial dysfunction and NADPH oxidase activation, which in turn activates the NF-κB signaling cascade *via* IκBα phosphorylation and degradation.[34] Activated NF-κB promotes the transcription of pro-inflammatory cytokines including TNF-α, IL-6, and IL-1β, which further amplify oxidative stress, establishing a self-reinforcing pathological cycle that delays tissue repair. To determine whether DL-JPatch can disrupt the ROS-inflammation amplification loop, we evaluated NF-κB expression, immune cell infiltration, and lipid peroxidation marker 4-HNE at the ulcer site. The untreated group showed markedly elevated NF-κB staining intensity compared with normal tissues, consistent with the persistent inflammatory state of the ulcer. Both CTA gel- and DL-JPatch-treated groups exhibited significantly lower NF-κB levels compared with DL-JPatch (-TA)-treated group, which showed only a partial reduction, suggesting relatively weaker suppression of inflammatory signaling (Fig. 6d, third row). To further examine inflammatory responses at the cellular level, CD11b immunostaining was performed to quantify infiltrating myeloid cells.[16] Normal tissues exhibited minimal CD11b-positive cells, compared with the extensive accumulation observed in untreated and CTA gel-treated groups. DL-JPatch (-TA) treatment led to only a modest reduction, whereas DL-JPatch detectably decreased CD11b-positive cell accumulation, approaching levels observed in normal tissues (Fig. 6d, fourth row). Quantitative analysis confirmed a significant reduction in inflammatory cell infiltration in the DL-JPatch group, while CTA gel did not significantly differ from the untreated control (Fig. S2b). These findings suggest that DL-JPatch not only suppresses inflammation but also promotes a more favorable immune microenvironment for tissue repair. Given the established role of oxidative stress in delaying oral mucosal healing, lipid peroxidation was evaluated by 4-hydroxynonenal (4HNE) staining. Both untreated and CTA gel-treated ulcers exhibited substantial 4HNE-positive regions, indicating persistent oxidative damage (Fig. 6d, fifth row). In contrast, 4HNE-positive areas were significantly reduced in the DL-JPatch (-TA) and DL-JPatch groups, indicating effective attenuation of oxidative stress at the wound site (Fig. 6d, fifth row). This reduction in lipid peroxidation provides strong evidence of the localized ROS-scavenging capability of the CeO_2-containing, genipin-crosslinked outer layer, which may further suppress ROS-mediated amplification of inflammatory signaling within the ulcer microenvironment.

Finally, semi-quantitative histological scoring was performed to integrate these findings. "Complete wound closure" was defined as full re-epithelialization with restoration of epithelial continuity and marker expression profiles (NF-κB, CD11b, 4HNE) comparable to those of healthy control tissue, as confirmed by H&E and immunohistochemical analyses (Fig. 6d, S2 and S3). By these criteria, the DL-JPatch group achieved near-complete histological restoration by Day 4, with marker expression values that were not statistically different from those of normal tissue, whereas the untreated, CTA gel-treated, and DL-JPatch (-TA)-treated groups remained significantly different from the healthy control across all assessed parameters (Fig. S3).

In summary, these results demonstrate DL-JPatch's superior therapeutic efficacy over conventional topical corticosteroid gel by integrating stable mucosal retention, localized anti-inflammatory drug delivery, and sustained redox regulation within a single Janus architecture. However, further studies are required to determine whether these therapeutic effects arise from synergistic interactions or combined additive effects.

Conclusions

In this study, cerium oxide nanoparticles-containing gallic acid-conjugated chitosan hydrogels crosslinked using genipin have been developed for the treatments of oral ulcers. These hydrogels showed rapid gelation behaviors by addition of genipin and excellent mechanical properties and stability *in vitro* and *in vivo*. In addition, the CHI-G/CeO_2/Gp hydrogels showed strong tissue adhesiveness and bursting pressures with biocompatibility that holding potential for versatile biomedical applications including wound dressing and healing materials. Furthermore, the triamcinolone acetonide-containing CHI-G/CeO_2/Gp hydrogels could accelerate the wound closure in oral defect animal models. Thus, these tissue adhesive genipin-crosslinked CeO_2-containing chitosan hydrogels can be a useful platform for the treatments of oral ulcers by reactive oxygen scavenging and local drug delivery. Given their localized and repeatable mode of application, this strategy may also hold translational potential for clinical conditions characterized by recurrent ulcer formation.

Author contributions

Han Sol Kim and Sujin Park: data curation, formal analysis, investigation, methodology, validation, visualization, writing – original draft, and writing – review & editing. Sang-woo Lee and Ji Hyun Ryu: conceptualization, data curation, formal analysis, investigation, methodology, project administration, supervision, validation, visualization, funding acquisition, writing – original draft, and writing – review & editing.

Conflicts of interest

The authors declare that there is no conflicts of interest.

Data availability

Data will be made available on request.

Supplementary information (SI): additional figures (Fig. S1–S3) presenting gelation kinetics, rheological analysis, immunohistochemical quantification, wound closure analysis, and histological scoring data, as well as supplementary tables (Tables S1–S2) describing histological scoring criteria and ICP-MS analysis results. See DOI: https://doi.org/10.1039/d6ra00275g.

Acknowledgements

This work was supported by a National Research Foundation of Korea (NRF) grant funded by the Korean Government (MSIT) (RS-2025-22802982, JHR) and a Korean Fund for Regenerative Medicine (KFRM) grant funded by the Korean Government (Ministry of Science and ICT and Ministry of Health & Welfare) (22A0103L1, JHR). This work was also supported by an NRF grant funded by the Korean Government (MSIT) (RS-2026-25487490, SL) and the Creative-Pioneering Researchers Program through Seoul National University (860-20250087).

References

1 S. T. Sonis, *Nat. Rev. Cancer*, 2004, **4**, 277–284.
2 X. Zeng, X. Jin, L. Zhong, G. Zhou, M. Zhong, W. Wang, Y. Fan, Q. Liu, X. Qi, X. Guan, Z. Yan, X. Shen, Y. Wu, L. Fan, Z. Wang, Y. He, H. Dan, J. Yang, H. Wang, D. Liu, H. Feng, K. Jiao and Q. Chen, *Int. J. Oral Sci.*, 2022, **14**, 28.
3 C. Scully, *N. Engl. J. Med.*, 2006, **355**, 165–172.
4 R. M. Vasconcelos, N. Sanfilippo, B. J. Paster, A. R. Kerr, Y. Li, L. Ramalho, E. L. Queiroz, B. Smith, S. T. Sonis and P. M. Corby, *J. Dent. Res.*, 2016, **95**, 725–733.
5 Y. Lee, S. Yoo, S. K. J. Lee, S. Lee, Y. Kim, H. Choi, S. Song, H. Yu, J. Lee, M.-R. Ok, H. Lee, N. Lee, S. Jun, T. Hyeon, S. I. Han and S. Lee, *ACS Appl. Mater. Interfaces*, 2025, **18**, 309–325.
6 D. Herrera, A. J. van Winkelhoff, P. Matesanz, K. Lauwens and W. Teughels, *Periodontol*, 2000, 2023.
7 V. Hearnden, V. Sankar, K. Hull, D. V. Juras, M. Greenberg, A. R. Kerr, P. B. Lockhart, L. L. Patton, S. Porter and M. H. Thornhill, *Adv. Drug Deliv. Rev.*, 2012, **64**, 16–28.
8 V. F. Patel, F. Liu and M. B. Brown, *J. Control. Release*, 2012, **161**, 746–756.
9 K. Anderson, R. L. Hamm, J. Am and C. Clin, *Wound Spec.*, 2012, **4**, 84–91.
10 C. Wicke, B. Halliday, D. Allen, N. S. Roche, H. Scheuenstuhl, M. M. Spencer, A. B. Roberts and T. K. Hunt, *Arch. Surg.*, 2000, **135**, 1265–1270.
11 C. Chen, Q. Zhang, W. Yu, B. Chang and A. D. Le, *J. Dent. Res.*, 2020, **99**, 1122–1130.
12 C. Estornut, G. Rinaldi, M. C. Carceller, S. Estornut and M. Pérez-Leal, *J. Mol. Med.*, 2024, **102**, 453–463.
13 Y. Zhang, L. Liu, X. Yu, H. Rong, W. Chen, J. Zhang, A. Dong, Z. Feng and S. Li, *Acta Biomater.*, 2024, **190**, 120–132.
14 H. S. Kim, M. Kim, Y. Kim, H. H. Shin, S.-W. Lee and J. H. Ryu, *Dent. Mater.*, 2024, **40**, 1970–1980.
15 H. Wu, F. Li, S. Wang, J. Lu, J. Li, Y. Du, X. Sun, X. Chen, J. Gao and D. Ling, *Biomaterials*, 2018, **151**, 66–77.
16 J. H. Ryu, J. S. Choi, E. Park, M. R. Eom, S. Jo, M. S. Lee, S. K. Kwon and H. Lee, *J. Control. Release*, 2020, **317**, 57–66.
17 B. Yang, Y. Chen and J. Shi, *Chem. Rev.*, 2019, **119**, 4881–4985.
18 S. I. Han, S.-W. Lee, M. G. Cho, J. M. Yoo, M. H. Oh, B. Jeong, D. Kim, O. K Park, J. Kim, E. Namkoong, J. Jo, N. Lee, C. Lim, M. Soh, Y.-E. Sung, J. Yoo, K. Park and T. Hyeon, *Adv. Mater.*, 2020, **32**, 2001566.
19 B. Lee, Y. Lee, N. Lee, D. Kim and T. Hyeon, *Nat. Rev. Mater.*, 2025, **10**, 252–267.
20 Y. G. Kim, Y. Lee, N. Lee, M. Soh, D. Kim and T. Hyeon, *Adv. Mater.*, 2024, **36**, 2210819.
21 I. Allu, A. K. Sahi, P. Kumari, K. Sakhile, A. Sionkowska and S. Gundu, *Micromachines*, 2023, **14**, 865.
22 A. García-Salvador, A. Katsumiti, E. Rojas, C. Aristimuño, M. Betanzos, M. Martínez-Moro, S. E. Moya and F. Goñi-de-Cerio, *Nanomaterials*, 2021, **11**, 1577.
23 L. Xu, J. Zhang, J. Luo, Y. Cui, J. Chen, B. Zeng, Z. Deng and L. Shao, *J. Nanobiotechnol.*, 2025, **23**, 387.
24 H. Liu, C. Liu, D. Shao, W. Li, X. Hu, J. Tian, L. Li, S. Ding, C. Zhou and L. Lu, *Chem. Mat.*, 2024, **36**, 4976–4989.
25 J. Xing, Y. Ding, X. Zheng, P. Yu, M. Qin, R. Qiu, Y. Li, S. Shang, J. Xie and J. Li, *Chem. Eng. J.*, 2022, **444**, 136580.
26 M. Xie, B. Hu, Y. Wang and X. Zeng, *J. Agric. Food Chem.*, 2014, **62**, 9128–9136.
27 K. Zhan, C. Kim, K. Sung, H. Ejima and N. Yoshie, *Biomacromolecules*, 2017, **18**, 2959–2966.
28 P. Guo, J. D. Anderson, J. J. Bozell and S. Zivanovic, *Carbohydr. Polym.*, 2016, **140**, 171–180.
29 S. L. Reay, E. L. Jackson, A. M. Ferreira, C. M. U. Hilkens and K. Novakovic, *Mater. Adv.*, 2022, **3**, 7946–7959.
30 M. F. Butler, Y.-F. Ng and P. D. A. Pudney, *J. Polym. Sci., Part A: Polym. Chem.*, 2003, **41**, 3941–3953.
31 F.-L. Mi, S.-S. Shyu and C.-K. Peng, *J. Polym. Sci., Part A: Polym. Chem.*, 2005, **43**, 1985–2000.
32 F.-L. Mi, H.-W. Sung and S.-S. Shyu, *J. Polym. Sci., Part A: Polym. Chem.*, 2000, **38**, 2804–2814.
33 S. Duanghathaipornsuk, F. A. O. Alateeq, S. S. Kim, D.-S. Kim and A. C. Alba-Rubio, *Sens. Actuator, B*, 2020, **321**, 128467.
34 M. J. Morgan and Z. Liu, *Cell Research*, 2011, **21**, 103–115.